





Correlating Visual Characteristics and Cryogenic Performance of Superconducting Detectors

K. R. Ferguson ^{a,b}, A. N. Bender ^{b,c,d}, N. Whitehorn ^e, and T. W. Cecil ^b

^aDepartment of Physics and Astronomy, University of California, Los Angeles, CA, 90095, USA

^bHigh-Energy Physics Division, Argonne National Laboratory, 9700 South Cass Avenue.,
Lemont, IL, 60439, USA

^cDepartment of Astronomy and Astrophysics, University of Chicago, 5640 South Ellis Avenue,
Chicago, IL, 60637, USA

^dKavli Institute for Cosmological Physics, University of Chicago, 5640 South Ellis Avenue,
Chicago, IL, 60637, USA

^eDepartment of Physics and Astronomy, Michigan State University, East Lansing, MI 48824,
USA

ABSTRACT

Cryogenic characterization of transition-edge sensor (TES) bolometers is a time- and labor-intensive process. As new experiments deploy larger and larger arrays of TES bolometers, the testing process will become more of a bottleneck. Thus it is desirable to develop a method for evaluating detector performance at room temperature. One possibility is using machine learning to correlate detectors' visual appearance with their cryogenic properties. Here, we use three engineering-grade TES bolometer wafers from the production cycle for SPT-3G, the current receiver on the South Pole Telescope, to train and test such an algorithm. High-resolution images of these TES bolometers were captured and relevant features were calculated from the images. Cryogenic performance metrics, including a detector's ability to tune and superconducting parameters such as normal resistance, critical temperature, and transition width, were also measured. A random forest algorithm was trained to predict these performance metrics from the visual features. Analysis of the images proved highly successful. While the ability of the random forest algorithm to predict cryogenic features was limited with the chosen set of input image features, it is possible that an increase in data volume or the addition of more image features will solve this problem.

Keywords: bolometer, detector, transition-edge sensors, machine learning, microscopy, cosmology, cryogenics

1. INTRODUCTION

Transition-edge sensor (TES) bolometers are widely used in state-of-the-art particle physics experiments as well as millimeter-wave and x-ray astronomical observations. When a bolometer absorbs energy, its temperature changes, prompting a change in its resistance. This change in resistance is read out to measure the signal on the sky. TES bolometers have superconducting thermistors that are voltage biased to operate precisely in their superconducting transition; thus, a small change in temperature yields a large change in resistance, enabling the detectors to be highly sensitive even to weak signals.^{1,2}

The experiments enabled by TES bolometers touch on some of the largest questions in cosmology and particle physics today. For example, experiments such as SPT-3G (the current receiver on the South Pole Telescope [SPT]), BICEP Array, Advanced ACTPol (the current receiver on the Atacama Cosmology Telescope [ACT]), POLARBEAR/Simons Array, and Simons Observatory use TES bolometers to precisely map the temperature and polarization anisotropies of the cosmic microwave background (CMB), the relic radiation leftover from the early universe.³⁻⁷ SuperCDMS-Soudan uses TES bolometers to search for scattering of weakly-interacting

Corresponding author: K. R. Ferguson

E-mail: kferguson@physics.ucla.edu

massive particles (WIMPs) off regular matter, and the SCUBA-2 experiment maps cold gas and dust in the universe using TES bolometers.^{8–10} Together, these experiments seek to determine the nature of dark matter and dark energy, to measure the precise value of the effective number of relativistic species, and to probe the universe’s inflationary period.^{11–17}

For CMB experiments, the dominant source of noise for TES bolometers is Poisson noise from photon counting statistics. This noise decreases as more photons are collected; while more photons could be collected by increasing the size of the detectors, this would degrade the angular resolution of the telescopes. Thus in order to build more sensitive experiments, larger arrays of TES bolometers must be deployed. For example, current-stage CMB experiments like SPT-3G and Advanced ACTPol deploy $\mathcal{O}(10,000)$ detectors, while the upcoming CMB-S4 experiment is expected to deploy $\mathcal{O}(500,000)$ to reach its science goals.^{18–20} Characterization and verification of bolometer performance is a time- and labor-intensive process. Each wafer of $\mathcal{O}(1,000)$ bolometers must be packaged with readout electronics into modules and installed into a cryogenic chamber. The chamber must cool the detectors to sub-Kelvin temperatures after which performance data can be captured. The electrical and thermal properties of a TES bolometer include (but are not limited to) resistance R , critical temperature T_c , thermal conductance G , and saturation power P_{sat} . Optical properties such as the bandpass, efficiency, and polarization sensitivity can also be measured during this stage. Typically, this testing process takes a minimum of two weeks, without much room for optimization in the steps outlined above. In the case of CMB-S4, characterizing the $\sim 500,000$ TES bolometers across several hundred wafers will be a significant undertaking.²¹ Therefore, it is desirable to flag under-performing wafers at room temperature before ever packaging them and installing them in a cryostat. As these larger detector arrays are deployed, this process would reduce time spent testing wafers that have a low probability of being used in an experiment.

Using detector wafers developed for SPT-3G, we attempt to correlate cryogenic performance of TES bolometers with optical images through a random forest machine learning (ML) algorithm. Section 2 of these proceedings describes the SPT-3G detector wafers and readout system used. Section 3 details the capturing of cryogenic data, and Section 4 explains the details of our imaging procedure. Section 5 covers the details of the analysis procedure and the ML algorithm used to correlate visual and performance data. Lastly, Section 6 covers the results and conclusions of the project.

2. DETECTOR & READOUT OVERVIEW

2.1 Detectors

For this initial exploration of the ML technique, we use three engineering-grade detector wafers from SPT-3G: W148, W162, and W187. SPT-3G is the third (and current) camera installed on the SPT, and it observes the CMB with 10 wafers of 1614 TES detectors each.²² See Ref. 3 for further details on the design and operation of SPT-3G. The bolometer architecture was fabricated on a silicon wafer via a multi-step lithographic process;^{23,24} Fig. 1 shows an example bolometer. Target TES properties for the SPT-3G fabrication process were:

- $80\mu\text{m}$ long by 15 or $20\mu\text{m}$ wide (the width was changed during the fabrication process, and so different wafers have different nominal TES widths)
- A normal resistance $R_n = 2.0$ Ohms
- A critical temperature $T_c = 450$ mK
- A saturation power P_{sat} of 10.2, 15.4, and 20.0 pW for detectors in the 95, 150, and 220 GHz observing band, respectively

2.2 Readout

The SPT-3G hardware utilizes a frequency-domain multiplexing readout system, detailed in Ref. 25 but summarized here. Each detector is placed in series with an LC resonator tuned to a frequency between 1 and 6 MHz; up to 68 of these channels are placed in parallel and read out simultaneously. The signal is amplified in a superconducting quantum interference device (SQUID) and nulled via a feedback loop to keep the SQUID from saturating. The measured outputs are demodulated using the known LC resonant frequencies.

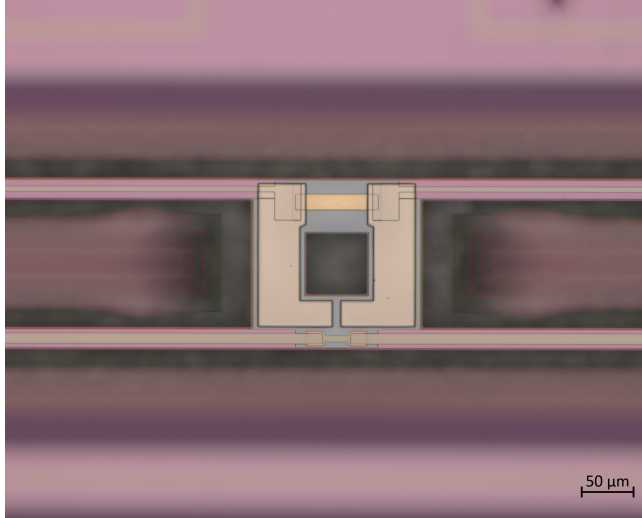


Figure 1. A TES bolometer on an SPT-3G detector wafer.

3. CRYOGENIC PERFORMANCE MEASUREMENTS

Data on the cryogenic performance of the detector wafers were captured using a cryogenic chamber with a Simon Chase* He-10 sorption cooler refrigerator backed by a Cryomech† PT415 cryocooler. The fridge is capable of reaching temperatures as low as 230 mK and the cold stage can house one SPT-3G detector wafer at a time. The cryostat is configured for dark measurements; the radiative loading on the detectors is limited by a cover that is held at the base operating temperature.

Once the detectors are cooled down, each readout channel must be mapped to an actual detector on the wafer. We perform such a network analysis by sending in a pure sinusoidal tone whose frequency is slowly swept through the entire possible LC range. Each bolometer has an expected resonant frequency defined by the LC that it is in series with. Expected frequencies are mapped to the measured ones, which are then used for the MHz biases in further detector operation.

3.1 Detector Tuning

Once the hardware mapping of all the detector and readout connections in the system is completed, we begin operation by tuning the SQUIDs. They are first heated up to ~ 16 K to remove any parasitic loop current residing within. After letting them cool, we set a current bias across each SQUID and measure the voltage across the SQUID V as we sweep through a range of flux biases ϕ . For a well-performing SQUID, this $V-\phi$ curve should be a sinusoid; we measure such a curve for a range of current biases, choosing to tune the SQUID to the current bias that yields the largest peak-to-peak amplitude in this sinusoid.

After we've tuned the SQUIDs, we attempt to *overbias* the bolometers. The detectors are brought up to 650 mK (above the detectors' target T_c). While the TES bolometers are in the normal regime, the MHz bias waveforms are initialized, the correct phase of the nulling signal is determined for each channel, and feedback is enabled. At the end of this process, the amplitude of the voltage bias is increased to the level required to maintain the TES in the normal regime. Any bolometer for which this procedure succeeds is labeled *overbiased*.

Lastly, we must tune the bolometers; that is, drop them into their superconducting transition and operate them. The temperature of the detectors is dropped below T_c while maintaining the overbiased state. The bias is then slowly lowered until each detector reaches the target fraction of its normal resistance (usually set to 80%).

*<https://www.chasecryogenics.com/>

†<https://www.cryomech.com/>

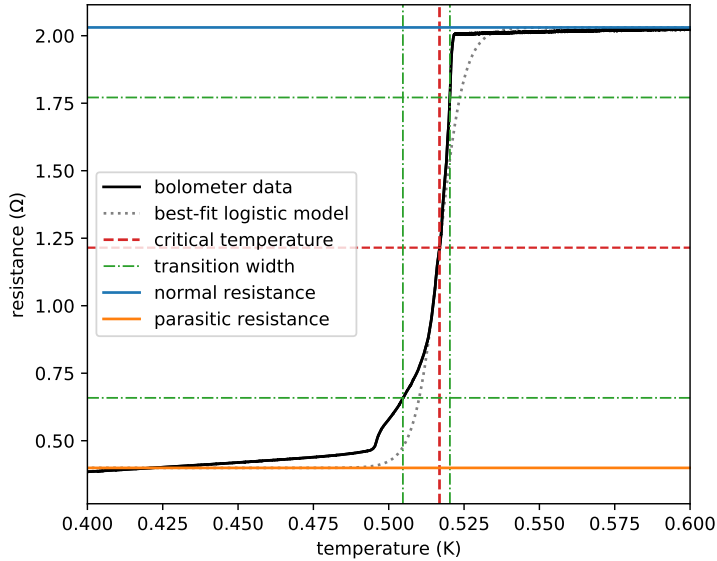


Figure 2. Resistance vs. temperature curve for an example bolometer. For each $R(T)$ curve, we determine the best-fit values for the critical temperature T_c (red dotted line), transition width ΔT_c (dot-dashed green line), normal resistance R_n (blue solid line), and parasitic resistance R_p (orange solid line). The logistic curve used to fit the parameters (Eqn. 1) is shown as the dotted gray line.

3.2 Detector Performance Characterization

Once we have verified that we can tune a bolometer, we can proceed to characterizing its performance. We measure two main quantities: resistance R as a function of temperature T and thermal conductance to the bath G .

To measure $R(T)$, the bolometers are overbiased at 650 mK with a minimal amplitude. Using the sorption fridge and supplemental heater, the detectors are slowly swept through a range of temperatures down to a minimum between 300 and 350 mK (various minimum temperatures were used to optimize some details of fridge control). Each detector’s readout timestream, originally in unitless DAQ counts, is converted to resistance using a factor derived from the readout system.²⁶ We measure the same while sweeping the temperature back up to 650 mK, giving us an up-timestream and a down-timestream for each bolometer.

For each timestream, we determine the best-fit values for R_n , T_c , the transition width ΔT_c , and the parasitic resistance R_p . These parameters are determined by fitting a logistic function of the form

$$R(T) = \frac{R_n}{1 + \exp[-d(T - T_0)]} + R_p \quad (1)$$

to the timestream. Here, T_0 is the center of the logistic function; it is a possible choice for T_c , though for rigor T_c is defined as the temperature where $R(T) = 0.5(R_n - R_p) + R_p$. The steepness of the logistic fit is given by d ; although it is related to ΔT_c , we treat it as a nuisance parameter. Instead, ΔT_c is defined asymmetrically around T_c ; the upper bound is the temperature where $R(T) = 0.841(R_n - R_p) + R_p$ (one standard deviation above center), and the lower bound is the temperature where $R(T) = 0.159(R_n - R_p) + R_p$ (one standard deviation below center). An example $R(T)$ curve showing the best-fit values is shown in Fig. 2. Fig. 3 shows histograms of the measured values for R_n , R_p , T_c , and the upper and lower bounds on ΔT_c , split by wafer.

Data are also captured measuring G . This is done by dropping the bolometers into their transition for a range of temperatures between 250 mK and 550 mK (for some detectors, the higher temperatures are above their T_c ; those points are ignored in the analysis). At each temperature, we measure the saturation power P_{sat} . For simplicity, information about P_{sat} and G is left out of this analysis and saved for future work.

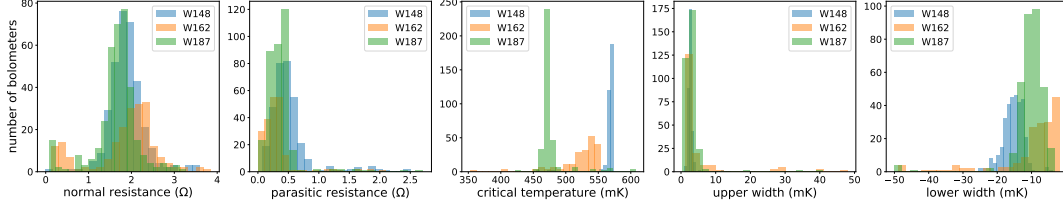


Figure 3. Cryogenic features determined from measuring resistance R as a function of temperature T .

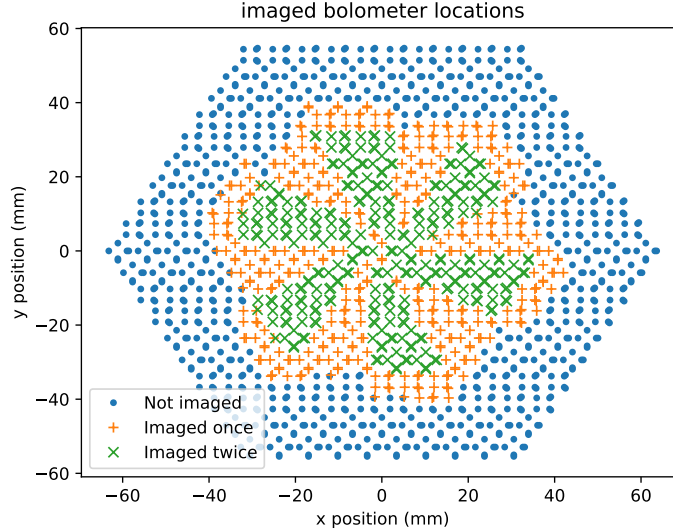


Figure 4. Bolometer locations relative to wafer center. Bolometers represented by blue dots were not imaged due to their proximity to the wafer edge. Bolometers represented by orange plus signs were imaged once and those represented by green exes were imaged twice.

4. IMAGING PROCEDURE

Optical images of the detectors were captured on a Zeiss Axio Imager Vario microscope housed at the Center for Nanoscale Materials at Argonne National Laboratory. The imaging process, including moving to each detector’s location, focusing, and capturing the image, was fully automated using the Zeiss ZEN Microscopy Software. Although the highest objective lens on this piece of equipment is 100x magnification, we elected to use the 20x objective lens as this allowed easier capture of the entire bolometer island architecture.³ Resulting images were 2752 pixels wide by 2208 pixels tall, with a scale factor of 0.227 microns per pixel. Images were captured in full color (see Fig. 1), although only their grayscale information was used for this analysis.

In the ideal case, images would be captured for every detector on a wafer. However, the SPT-3G detector wafers used here were packaged into modules, ready for cryogenic characterization. Part of the module housing is a holding structure allowing them to be mounted in the refrigerator. It was impossible to remove all of this structure without breaking the wirebonds connecting the wafer to the cables that attach to the readout LC chips. Due to the size of the objective lens, we could not image detectors near the edge of the wafer without colliding with the remaining housing structure; thus, boundaries had to be set on where we could take images. These boundaries were set conservatively to avoid all possibility of a collision. In total we were able to image about 44% of the detectors (that is, ~ 713 detectors) on each wafer. Due to the limited available imaging region, images were captured in six groups, with the wafer physically rotated underneath the microscope between each group. These groups partially overlapped, causing 42% of the imaged detectors (~ 300 detectors per wafer) to be imaged twice. The locations of the singly- and doubly-imaged detectors are shown in Fig. 4.

Additional challenges are inherent to the imaging process. The bolometer island is suspended over a trough as a result of the fabrication process. Occasionally, the microscope autofocus procedure will focus on this trough

rather than the bolometer itself. This reduces our usable data volume, but only by $\lesssim 10$ bolometers per wafer. Another consequence of this geometry is that some bolometers ($\lesssim 5\%$ on a single wafer) are not quite flat relative to the rest of the wafer. This is due to differing tension in the legs holding up the bolometer island on either side. For these detectors, the level of focus is a gradient across the island. In most cases, this adds some variance to the features we calculate from the images (Section 5), though in extreme cases it can lead to a failure to calculate any features at all.

Because the details of the bolometer island legs affect the thermal conductance G of the bolometer, we expect that the severity of this gradient will correlate with G . As previously stated, this consideration is left for future work.

5. ANALYSIS

In an ideal scenario, a machine learning algorithm would train directly on the images described in Section 4. However, this proved unfeasible with the amount of data available. While there are $\mathcal{O}(1,000,000)$ pixels per image, images were only captured for $\mathcal{O}(1,000)$ bolometers across the three wafers. Training directly on the images would yield an algorithm prone to overfitting, and one that would likely do a poor job estimating the properties of bolometers that were not used in the training set. For this reason, it was necessary to determine a set of features that could be calculated from the images and use those as inputs to the ML algorithm.

5.1 Image Feature Determination

All of the derived features require determining where the TES lies in the image. Due to varying orientation angle, drift of the wafer relative to the stage during the imaging process, and slight fabrication variance, this is not as trivial as simply picking out the same pixels in every image. The process for determining the TES location is shown step-by-step in Fig. 5. We first cut out a patch from the center of the image of size 1376×1104 pixels (half the size of the original image in each dimension) and convert the image to grayscale (Fig. 5a). We then apply a Meijering edge detection filter to the image (Fig. 5b).²⁷ The resulting array is binarized, with all pixels whose values are less than 20% of the maximum set to zero, and all other pixels set to one.

This binary mask is *skeletonized* (Fig. 5c), a process by which all of the detected edges are converted to be a single pixel wide (the width of the edges has been artificially increased in Fig. 5c for visibility). The skeleton can then be directly compared to a template (generated from the fabrication layout) of the most prominent lines on the bolometer island. The location and orientation angle of the template that give the highest correlation with the skeleton are used to determine the TES location in the image from its location in the template. First, we determine the angle by taking a probabilistic Hough transform²⁸ of the skeleton (Fig. 5d). Since the resulting line segments are mostly orthogonal or parallel to each other, we can divide them into two groups by their angle (Fig. 5e). We expect more lines in the horizontal direction (relative to the TES) than the vertical, so this gives us the orientation angle of the template up to a 180-degree modulus. For the two remaining possible orientation angles, we perform a matched filter between the template and the skeleton (Fig. 5f). The location of the maximum-valued pixel gives us both the offset from center and the orientation angle of the template.

To identify the line segments corresponding to the TES edges, we must have some foreknowledge of where we expect the TES to be. As a consequence of the matched filter, we already know this; since we know which lines in the template correspond to the TES edges, we then have an expected location within the image for the TES. We construct a 15-pixel buffer region around each expected line location and select the longest Hough line in said region to represent the true edge in the image. In addition to the TES edges, we identify Hough lines corresponding to the lines where the bling and lead intersect with the TES. These found lines define three regions, which are shown in Fig. 5h. Because the probabilistic Hough transform is random by nature, it returns a different set of line segments every time it is run on an identical skeleton. We run this process on each image 100 times and use the average vertex location to calculate our features.

14 features are calculated per image:

- We calculate the area and perimeter of the TES (*region one*, red lines in Fig. 5h), as well as the areas and perimeters of the smaller regions not covered by the lead (*region two*, aqua lines in Fig. 5h) and the bling (*region three*, green lines in Fig. 5h).

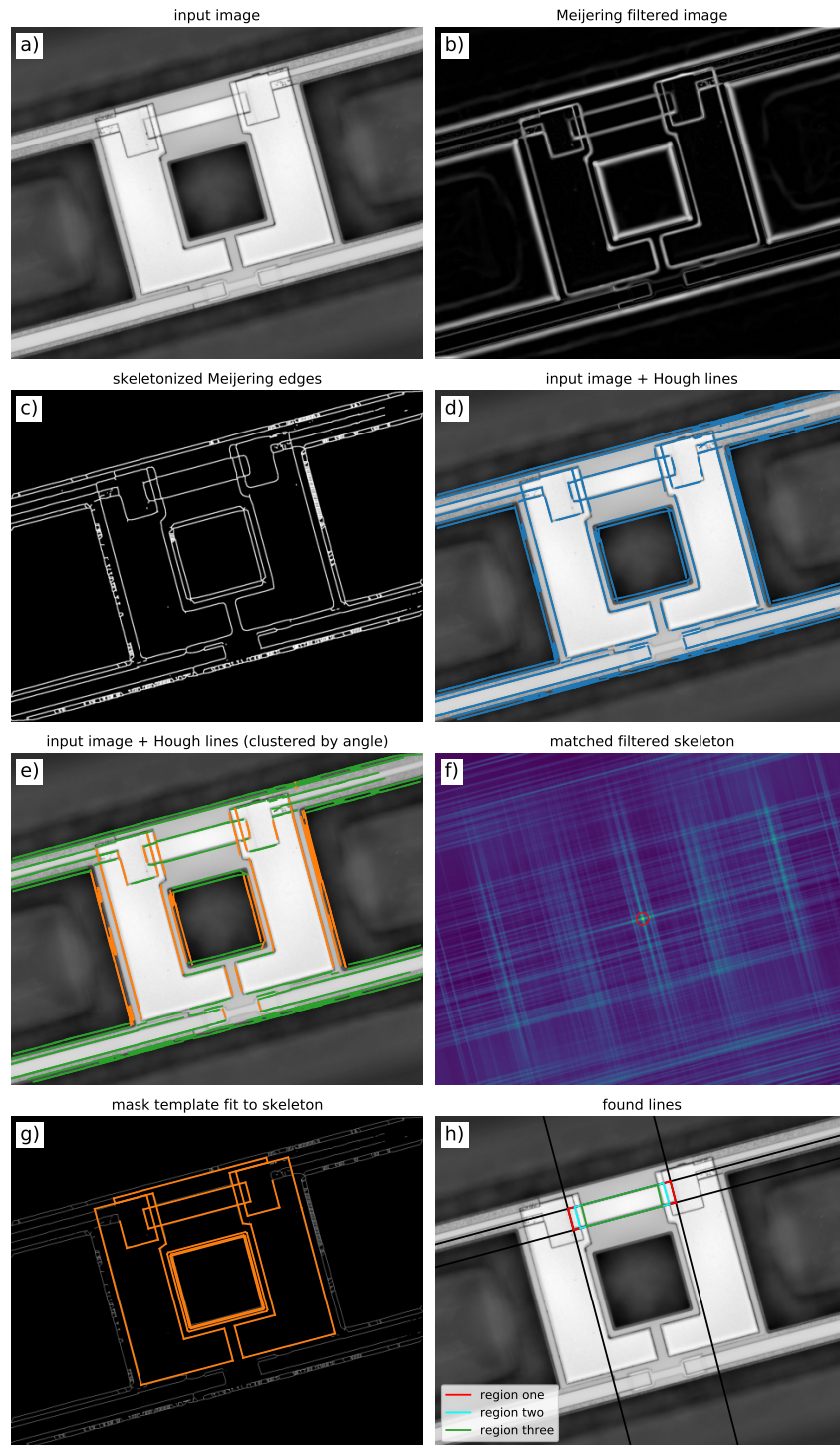


Figure 5. Step-by-step process of determining the location of the TES in an image. a) The image is trimmed around the center and converted to grayscale. b) The image is filtered with a Meijering edge detection algorithm. c) The Meijering edges are skeletonized to become a single pixel wide. d) Probabilistic Hough lines are calculated from the skeleton. e) The Hough lines are divided by angle into two groups to determine the overall angle of the TES. f) A template of the most prominent lines on the bolometer island is matched filtered with the skeleton to find the exact location and orientation. g) Best-fit template overlaid on the skeleton. h) Final lines found for TES edges, as well as overlap with other parts of the bolometer island.

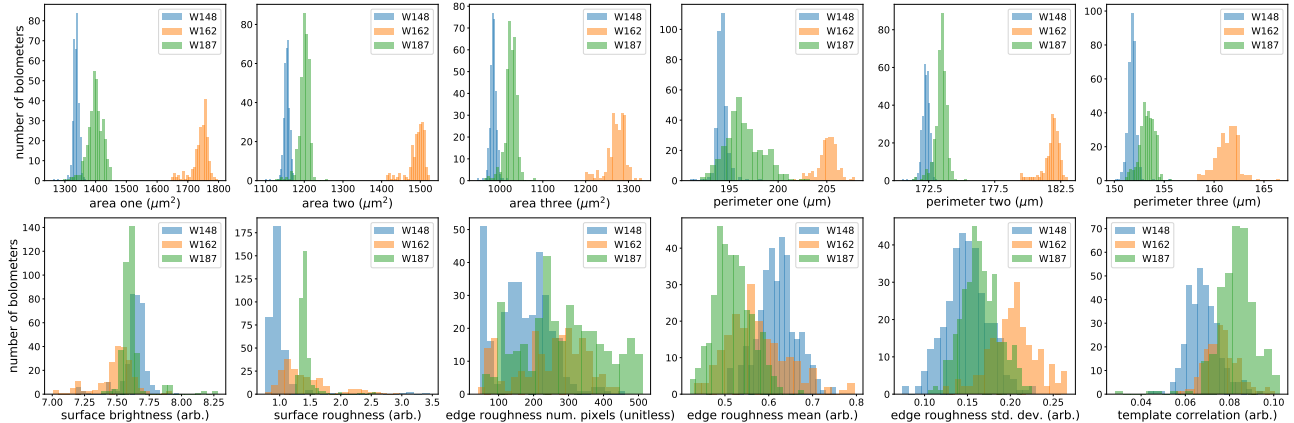


Figure 6. Image features (except for the TES angle and the flag for missing features) split by wafer. The label *one* (*two*) [*three*] for the area and perimeter features represents the full TES (region of the TES not overlapped by the lead) [region of the TES not overlapped by anything else]; see Fig. 5h for visual clarification. *Surface brightness/roughness* are the mean/standard deviation of the values of the pixels in region three. *Edge roughness* denotes the number of local maxima pixels, as well as their mean and standard deviation, for region one of the Meijering-filtered image. *Template correlation* denotes the maximum value of the matched-filtered skeleton with the bolometer island template.

- We estimate the roughness of the detector surface by calculating the mean and standard deviation of the pixel values within region three.
- Additionally, we quantify the roughness of the TES edges. This can be affected by detritus accumulating along the TES edges or by slight fabrication non-idealities. To estimate the roughness, we identify the pixels at which the Meijering-filtered image takes on local maxima in the vicinity of the TES. We measure the number of these pixels as well as the mean and standard deviation of their values (these quantities were shown to roughly correlate with the roughness of the TES edges in visual inspection).
- Occasionally, pieces of the bolometer architecture (such as the bling that serves to dissipate heat) are missing or obscured in the image. In these cases, we expect the matched filter between the template and the skeletonized image to return a smaller maximum value. To provide information on bolometers where this happens, we take this maximum value as a feature.
- Because some of the metrics described above are dependent on pixelization effects that differ at different angles, we also include the orientation angle of the TES as a feature.
- Lastly, occasional failures of the location-finding algorithm (usually due to either poor focus or missing pieces of the bolometer architecture) will lead to missing values for some or all features on a given detector. These values are imputed using the MissForest algorithm,²⁹ but in order to include some information about these failures we include a binary flag for whether there were any missing values before the imputation.

As discussed in Section 4, a subset of bolometers were imaged twice at different angles. For each subgroup of data on which we train an ML algorithm, two algorithms are actually trained: one in which the features from the doubly-imaged bolometers are kept, and one in which they are averaged. In the case where they are averaged, *all* features are averaged, even the angle and the binary flag for whether there were missing values before the data imputation. Fig. 6 histograms the value of all input features (except the angle and the binary flag). In these histograms, features from doubly-imaged bolometers are averaged and values imputed using MissForest are not included.

5.2 Machine Learning Algorithm

There are two main predictors of a wafer’s experimental viability: its detector yield and the performance of those detectors. We wish to predict both of these. For the first, we train a random forest classification algorithm; for the second, a random forest regression algorithm.³⁰ In both cases, we train on multiple subgroups of data:

- Individual wafer performance (80/20 train/test split)
- Train on two wafers, test the third
- Train on all wafers, with a random 20% of bolometers chosen for testing

Every time an algorithm is trained, algorithm hyperparameters are decided via an exhaustive grid search. Four hyperparameters are varied: the number of trees in the random forest $N_{\text{trees}} \in [10, 50, 100, 500, 1000]$, the maximum depth of each tree $d \in [1, 2, 3, 4, 5, 6]^{\ddagger}$, the minimum number of bolometers required to split an internal node on a tree $s \in [2, 3, 4]$, and the fraction of bolometers (with replacement) used to train each tree $f_{\text{bolos}} \in [0.1, 0.25, 0.5, 1.0]$. For each combination of hyperparameters, the algorithm performance is validated via five-fold cross validation.³¹ The training set is randomly split into five subgroups; each subgroup is in turn left out of training and used to determine a performance score, with the overall score for that combination of hyperparameters being the mean of the scores for all five subgroups. The final sets of hyperparameters used for each predictor are listed in the tables in Appendix A.

To classify detector yield, the bolometers are grouped into one of three categories: fully tuneable, able to overbias but not tune, and able to do neither. Because the percentage of bolometers in each class is not equal, we specifically perform a stratified cross validation here in which the ratio of bolometer classes is retained when splitting the training set into subgroups during cross validation. A simple classification accuracy was used to score performance.

Six output features y were used to characterize detector performance: R_n , R_p , T_c , and the one-standard-deviation-up and -down temperatures described in Section 3. As with the input features calculated from the images, some of these features are occasionally missing for a given bolometer. Missing values are imputed using the MissForest algorithm, and an additional feature flagging on whether there were any missing features before the imputation is included. The training data is scored with the R^2 coefficient, $R^2 \equiv 1 - \frac{u}{v}$, where $u = \sum_i (y_{\text{true}, i} - y_{\text{predicted}, i})^2$ and $v = \sum_i (y_{\text{true}, i} - \bar{y}_{\text{true}, i})^2$, and where the bar signifies the mean over the test set. Each output feature is scored separately, and the overall score is given by the mean of the scores in all six features.

Interpreting the training scores of the various algorithms requires the context of how they would perform if there were no correlation between the input features and the output classes/features. In order to quantify this, we shuffle the output classes/features in both the training and test sets and re-train/re-test the random forest on the shuffled data. The same set of input features is used, and the training/test sets are shuffled together. This is done 100 times and the mean and standard deviation of the resultant scores are used to estimate the no-skill performance of the algorithm.

6. RESULTS & DISCUSSION

The results for the random forest classification are shown in Table 1, and the results for the random forest regression in Table 2. The rows labeled *True* give the scores from the real training/test data, while the rows labeled *Shuffled* give the mean and the standard deviation of the scores of the shuffled data as described in Section 5. These results are visualized in Fig. 7.

Generally, the results are fairly insensitive to the specific treatment of doubly-imaged bolometers. The main exception is in the classification accuracies for the *Train W148+W187, Test W162* predictor. However, given the size of the *Shuffled* error bars and the similarity between *Kept/Averaged* cases in other predictors, it is likely this is due to statistical scatter rather than a real effect.

In most cases, a predictor’s *True* score is not meaningfully different from its mean *Shuffled* score, implying that the random forest lacks predictive power. However, the *True* scores are significantly lower than the mean *Shuffled* scores for many of the predictors where the algorithm is trained on data from two wafers and tested on data from a third. This discrepancy is moderate for the classification problem, but especially significant for

[‡]Initially, unlimited tree depth was an option. However, examination of algorithm learning curves determined that this led to overfitting and so the option was removed.

Table 1. Random forest classification performance results. The *True* scores are from the actual data while the *Shuffled* scores are the mean plus/minus the standard deviation of 100 training/test iterations where the output classes were randomly shuffled. All predictors use an 80/20 training/test split unless stated otherwise.

Classification Accuracy			
ML Predictor		Features for bolometers with two images	
		Kept	Averaged
W148 only	True	0.6281	0.6627
	Shuffled	0.6358 ± 0.0356	0.6199 ± 0.0472
W162 only	True	0.7013	0.6852
	Shuffled	0.6978 ± 0.0466	0.6669 ± 0.0568
W187 only	True	0.5430	0.5673
	Shuffled	0.4797 ± 0.0375	0.4991 ± 0.0471
Train W148+W162, Test W187	True	0.5258	0.5367
	Shuffled	0.6034 ± 0.0142	0.5990 ± 0.0155
Train W148+W187, Test W162	True	0.5459	0.2772
	Shuffled	0.5292 ± 0.1201	0.5624 ± 0.0828
Train W162+W187, Test W148	True	0.3261	0.2530
	Shuffled	0.5934 ± 0.0363	0.5599 ± 0.0689
All wafers, random train/test	True	0.6178	0.6083
	Shuffled	0.6013 ± 0.0226	0.5996 ± 0.0289

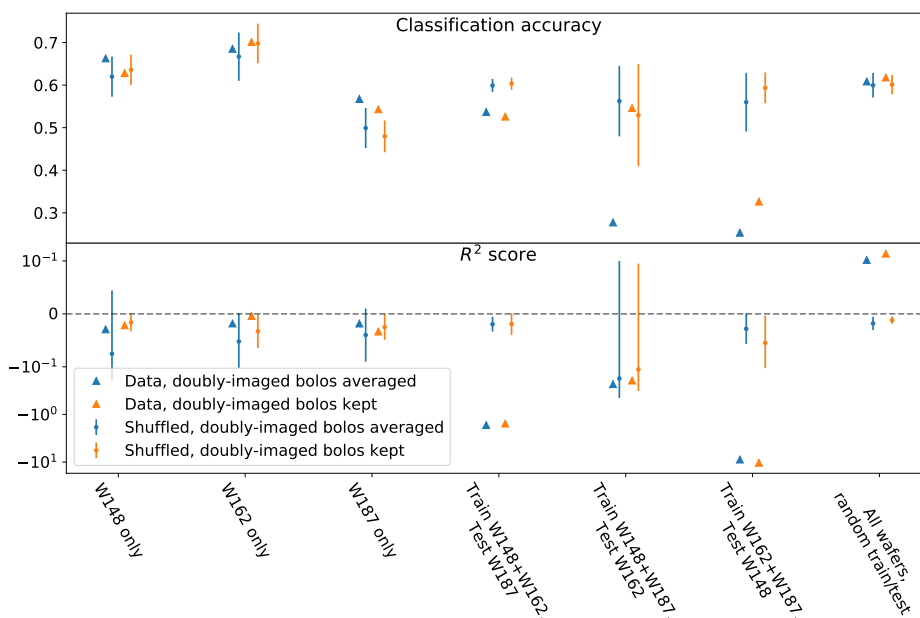


Figure 7. Visualization of the results displayed in Tables 1 and 2.

Table 2. Random forest regression performance results. The *True* scores are from the actual data while the *Shuffled* scores are the mean plus/minus the standard deviation of 100 training/test iterations where the output classes were randomly shuffled. All predictors use an 80/20 training/test split unless stated otherwise.

R^2 score			
ML Predictor		Features for bolometers with two images	
		Kept	Averaged
W148 only	True	-0.0216	-0.0292
	Shuffled	-0.0161 ± 0.0168	-0.0755 ± 0.1198
W162 only	True	-0.0040	-0.0182
	Shuffled	-0.0328 ± 0.0317	-0.0521 ± 0.0534
W187 only	True	-0.0335	-0.0183
	Shuffled	-0.0249 ± 0.0240	-0.0400 ± 0.0502
Train W148+W162, Test W187	True	-1.5543	-1.6732
	Shuffled	-0.0195 ± 0.0205	-0.0196 ± 0.0140
Train W148+W187, Test W162	True	-0.1947	-0.2316
	Shuffled	-0.1141 ± 0.2090	-0.1761 ± 0.2760
Train W162+W187, Test W148	True	-10.3544	-8.8573
	Shuffled	-0.0548 ± 0.0514	-0.0282 ± 0.0287
All wafers, random train/test	True	0.1207	0.1046
	Shuffled	-0.0175 ± 0.0099	-0.0180 ± 0.0125

the regression problem. This behavior arises because many of the input features are tri-modal (see Fig. 6); each wafer exhibits its own behavior (even among those with supposedly identical fabrication specifications), and features vary much more wafer-to-wafer than within individual wafers. Random forests do not perform well on data with input features outside of the training set, hence the poor predictions.

The most statistically-significant instance of a predictor performing better than random guessing is the *All wafers, random test/train* regression predictor. This is also the only regression predictor to have a positive score; that is, to do better than it would had it simply guessed the test set mean for every feature. It is tempting to ascribe this increase in performance to the fact that more data are used to train the algorithm. However, due to the tri-modality described above, the random forest is essentially predicting which wafer a bolometer is on (with high precision) and assigning it the mean output features from that wafer. While having this predictive power indicates that the random forest algorithm is in some way performing as it should, it is less useful for real-world applications, where the goal is to accurately predict cryogenic features of detectors on wafers that were not used in the training set. This is perhaps not surprising; given that feature variation is much larger between wafers than within them, our effective sample size is much reduced. Many more wafers would be needed to begin predicting full-wafer features.

Future work on this topic can expand on the current study in a number of ways:

- As with any ML problem, the collection of more data is likely to yield better results with stronger predictive power.
- This study has focused on only a limited amount of the visual information available in the bolometer images. Calculating more input features (or even finding a way to train on the images themselves while

still avoiding overfitting) could prove informative.

- This study used an “out-of-the-box” measure of classification accuracy. Changing the decision threshold by optimizing precision/recall (or, equivalently, the F_1 score) in a one-vs-all or one-vs-one classification scheme could yield better performance.
- Bolometer performance depends on more than the limited set of output features predicted in the regression algorithms. Future work should incorporate information on the thermal conductance G , the saturation power P_{sat} , and perhaps even optical bolometer properties.

Although it is unclear how much data must be included in the training set before the random forests that were trained gain predictive power on new detector wafers, the algorithms were extremely successful at predicting which wafer a bolometer belonged to. Furthermore, the image analysis proved adept at revealing previously unknown defects. Even without predictive power from a machine learning algorithm, the image analysis holds potential for identifying potentially flawed detectors prior to cryogenic characterization. Finally, we note that the image analysis is easily generalized to other detector geometries for use in future experiments.

APPENDIX A

Here we include the optimal set of hyperparameters that were determined for each of the random forests that were trained. Table 3 lists those determined for the classification algorithms, and Table 4 the regression algorithms.

Table 3. Optimal random forest hyperparameters for classification. N_{trees} is the number of trees in the random forest; choices were [10, 50, 100, 500, 1000]. d is the maximum allowed depth of each tree; choices were [1, 2, 3, 4, 5, 6]. s is the minimum number of bolometers necessary to split a node on the tree; choices were [2, 3, 4]. f_{bolos} is the fraction of the total number of bolometers used to train each tree, chosen with replacement from the full set; choices were [0.1, 0.25, 0.5, 1.0].

Classification Hyperparameters					
ML Predictor	Features for bolometers with two images	Hyperparameters			
		N_{trees}	d	s	f_{bolos}
W148 only	Kept	10	4	2	0.25
	Averaged	50	4	3	0.25
W162 only	Kept	10	2	3	1.0
	Averaged	10	2	2	1.0
W187 only	Kept	10	6	2	0.25
	Averaged	10	5	2	0.5
Train W148+W162, Test W187	Kept	100	6	4	0.25
	Averaged	50	6	3	0.1
Train W148+W187, Test W162	Kept	50	6	2	1.0
	Averaged	500	6	2	0.25
Train W162+W187, Test W148	Kept	500	6	4	0.5
	Averaged	50	6	4	0.25
All wafers, random train/test	Kept	10	5	4	1.0
	Averaged	50	6	4	1.0

Table 4. Optimal random forest hyperparameters for classification. N_{trees} is the number of trees in the random forest; choices were [10, 50, 100, 500, 1000]. d is the maximum allowed depth of each tree; choices were [1, 2, 3, 4, 5, 6]. s is the minimum number of bolometers necessary to split a node on the tree; choices were [2, 3, 4]. f_{bolos} is the fraction of the total number of bolometers used to train each tree, chosen with replacement from the full set; choices were [0.1, 0.25, 0.5, 1.0].

Regression Hyperparameters					
ML Predictor	Features for bolometers with two images	Hyperparameters			
		N_{trees}	d	s	f_{bolos}
W148 only	Kept	50	1	3	1.0
	Averaged	10	1	4	0.5
W162 only	Kept	50	1	2	0.25
	Averaged	100	1	3	0.1
W187 only	Kept	10	3	3	1.0
	Averaged	10	1	4	0.5
Train W148+W162, Test W187	Kept	100	5	2	1.0
	Averaged	100	5	2	1.0
Train W148+W187, Test W162	Kept	50	2	3	1.0
	Averaged	100	3	4	1.0
Train W162+W187, Test W148	Kept	500	5	2	1.0
	Averaged	1000	3	3	1.0
All wafers, random train/test	Kept	1000	6	3	1.0
	Averaged	500	6	2	1.0

ACKNOWLEDGMENTS

The authors would like to thank Claudio Kopper, Matthew Becker, Nesar Ramachandra, and Markus Rau for their helpful conversations, as well as the SPT-3G collaboration for the use of their detector wafers for this study. The South Pole Telescope program is supported by the National Science Foundation (NSF) through grants PLR-1248097, OPP-1852617. Work at Argonne, including use of the Center for Nanoscale Materials, an Office of Science user facility, was supported by the U.S. Department of Energy, Office of Science, Office of Basic Energy Sciences and Office of High Energy Physics, under Contract No. DE-AC02-06CH11357. We gratefully acknowledge the computing resources provided on Crossover, a high-performance computing cluster operated by the Laboratory Computing Resource Center at Argonne National Laboratory. KF acknowledges support from the U.S. Department of Energy’s Office of Science Graduate Student Research (SCGSR) Program. This work makes use of the `numpy`,³² `matplotlib`,³³ `scipy`,³⁴ `scikit-image`,³⁵ and `scikit-learn`³⁶ Python packages.

REFERENCES

- [1] Richards, P. L., “Bolometers for infrared and millimeter waves,” *Journal of Applied Physics* **76**, 1–24 (July 1994).
- [2] Irwin, K. D. and Hilton, G. C., “Transition-Edge Sensors,” in [*Cryogenic Particle Detection*], Enns, C., ed., **99**, 63 (2005).
- [3] Sobrin, J. A. et al., “The Design and Integrated Performance of SPT-3G,” *Astrophys. J. Supp.* **258**(2), 42 (2022).

- [4] Moncelsi, L. et al., “Receiver development for BICEP Array, a next-generation CMB polarimeter at the South Pole,” in [*Society of Photo-Optical Instrumentation Engineers (SPIE) Conference Series*], *Society of Photo-Optical Instrumentation Engineers (SPIE) Conference Series* **11453**, 1145314 (Dec. 2020).
- [5] Crowley, K. T. et al., “Advanced ACTPol TES Device Parameters and Noise Performance in Fielded Arrays,” *J. Low Temp. Phys.* **193**(3-4), 328–336 (2018).
- [6] Westbrook, B. et al., “The POLARBEAR-2 and Simons Array Focal Plane Fabrication Status,” *Journal of Low Temperature Physics* **193**, 758–770 (Dec. 2018).
- [7] Collaboration, S. O., “The Simons Observatory: science goals and forecasts,” *Journal of Cosmology and Astroparticle Physics* **2019**, 056 (Feb. 2019).
- [8] Agnese, R., others, and SuperCDMS Collaboration, “Results from the Super Cryogenic Dark Matter Search Experiment at Soudan,” *Phys. Rev. Lett.* **120**, 061802 (Feb. 2018).
- [9] Holland, W. S. et al., “SCUBA-2: The 10000 pixel bolometer camera on the James Clerk Maxwell Telescope,” *Mon. Not. Roy. Astron. Soc.* **430**, 2513 (2013).
- [10] Mairs, S. et al., “A decade of SCUBA-2: A comprehensive guide to calibrating 450 μm and 850 μm continuum data at the JCMT,” *The Astronomical Journal* **162**, 191 (oct 2021).
- [11] Abazajian, K. N. et al., “Neutrino Physics from the Cosmic Microwave Background and Large Scale Structure,” *Astropart. Phys.* **63**, 66–80 (2015).
- [12] Weinberg, S., “Goldstone Bosons as Fractional Cosmic Neutrinos,” *Phys. Rev. Lett.* **110**(24), 241301 (2013).
- [13] Lesgourgues, J. and Pastor, S., “Massive neutrinos and cosmology,” *Phys. Rept.* **429**, 307–379 (2006).
- [14] Guth, A. H., “The Inflationary Universe: A Possible Solution to the Horizon and Flatness Problems,” *Phys. Rev. D* **23**, 347–356 (1981).
- [15] Lyth, D. H., “What would we learn by detecting a gravitational wave signal in the cosmic microwave background anisotropy?,” *Phys. Rev. Lett.* **78**, 1861–1863 (1997).
- [16] Abazajian, K. N. et al., “Inflation Physics from the Cosmic Microwave Background and Large Scale Structure,” *Astropart. Phys.* **63**, 55–65 (2015).
- [17] Bucher, M., “Physics of the cosmic microwave background anisotropy,” *Int. J. Mod. Phys. D* **24**(02), 1530004 (2015).
- [18] Abazajian, K. N. et al., “CMB-S4 Science Book, First Edition,” (10 2016).
- [19] Abitbol, M. H. et al., “CMB-S4 Technology Book, First Edition,” (6 2017).
- [20] Abazajian, K. o., “CMB-S4 Science Case, Reference Design, and Project Plan,” *arXiv e-prints*, arXiv:1907.04473 (July 2019).
- [21] for the CMB-S4 Collaboration, D. R. B., “Conceptual design of the modular detector and readout system for the cmb-s4 survey experiment,” in [*Astronomical Telescopes and Instrumentation*], *Proc. SPIE* **12190-16** (2022).
- [22] Carter, F. W. et al., “Tuning SPT-3G Transition-Edge-Sensor Electrical Properties with a Four-Layer Ti-Au-Ti-Au Thin-Film Stack,” *Journal of Low Temperature Physics* **193**, 695–702 (Dec. 2018).
- [23] Posada, C. M. et al., “Fabrication of large dual-polarized multichroic TES bolometer arrays for CMB measurements with the SPT-3G camera,” *Superconductor Science Technology* **28**, 094002 (Sept. 2015).
- [24] Posada, C. M. et al., “Fabrication of Detector Arrays for the SPT-3G Receiver,” *Journal of Low Temperature Physics* **193**, 703–711 (Dec. 2018).
- [25] Bender, A. N. et al., “On-Sky Performance of the SPT-3G Frequency-Domain Multiplexed Readout,” *J. Low Temp. Phys.* **199**(1-2), 182–191 (2019).
- [26] Montgomery, J., *Digital frequency domain multiplexing readout: design and performance of the SPT-3G instrument and LiteBIRD*, PhD thesis, Montreal, Quebec, Canada (2021).
- [27] Meijering, E., Jacob, M., Sarria, J.-C., Steiner, P., Hirling, H., and Unser, M., “Design and validation of a tool for neurite tracing and analysis in fluorescence microscopy images,” *Cytometry Part A* **58A**(2), 167–176 (2004).
- [28] Galamhos, C., Matas, J., and Kittler, J., “Progressive probabilistic hough transform for line detection,” in [*Proceedings. 1999 IEEE Computer Society Conference on Computer Vision and Pattern Recognition (Cat. No PR00149)*], **1**, 554–560 Vol. 1 (1999).

- [29] Stekhoven, D. J. and Buehlmann, P., “Missforest - non-parametric missing value imputation for mixed-type data,” *Bioinformatics* **28**(1), 112–118 (2012).
- [30] Breiman, L., “Random Forests,” *Machine Learning* **45**(1), 5–32 (2001).
- [31] Stone, M., “Cross-validated choice and assessment of statistical predictions,” *Journal of the royal statistical society: Series B (Methodological)* **36**(2), 111–133 (1974).
- [32] Harris, C. R. et al., “Array programming with NumPy,” *Nature* **585**, 357–362 (Sept. 2020).
- [33] Hunter, J. D., “Matplotlib: A 2d graphics environment,” *Computing in Science & Engineering* **9**(3), 90–95 (2007).
- [34] Virtanen, P. et al., “SciPy 1.0: Fundamental Algorithms for Scientific Computing in Python,” *Nature Methods* **17**, 261–272 (2020).
- [35] van der Walt, S. et al., “scikit-image: image processing in Python,” *PeerJ* **2**, e453 (6 2014).
- [36] Pedregosa, F. et al., “Scikit-learn: Machine learning in Python,” *Journal of Machine Learning Research* **12**, 2825–2830 (2011).